Pore-space structure and average dissolution rates: A simulation study

J. P. Pereira Nunes[1,2], B. Bijeljic[1], and M. J. Blunt[1]

[1]Department of Earth Science and Engineering, Imperial College London, London, UK, [2]Reservoir Geophysics Group, Petrobras S.A., Rio de Janeiro, Brazil

Abstract We study the influence of the pore-space geometry on sample-averaged dissolution rates in millimeter-scale carbonate samples undergoing reaction-controlled mineral dissolution upon the injection of a CO_2-saturated brine. The representation of the pore space is obtained directly from micro-CT images with a resolution of a few microns. Simulations are performed with a particle tracking approach on images of three porous rocks of increasing pore-space complexity: a bead pack, a Ketton oolite, and an Estaillades limestone. Reactive transport is simulated with a hybrid approach that combines a Lagrangian method for transport and reaction with the Eulerian flow field obtained by solving the incompressible Navier-Stokes equations directly on the voxels of three-dimensional images. Particle advection is performed with a semianalytical streamline method and diffusion is simulated via a random walk. Mineral dissolution is defined in terms of the particle flux through the pore-solid interface, which can be related analytically to the batch (intrinsic) reaction rate. The impact of the flow heterogeneity on reactive transport is illustrated in a series of simulations performed at different flow rates. The average dissolution rates depend on both the heterogeneity of the sample and on the flow rate. The most heterogeneous rock may exhibit a decrease of up to two orders of magnitude in the sample-averaged reaction rates in comparison with the batch rate. Furthermore, we provide new insights for the dissolution regime that would be traditionally characterized as uniform. In most cases, at the pore-scale, dissolution preferentially enlarges fast-flow channels which greatly restricts the effective surface available for reaction.

1. Introduction

The flow of reactive fluids through geologic reservoirs is a complex phenomenon that occurs over a wide range of spatial and temporal scales. There is a strong coupling between flow and reaction, not directly described in terms of an ideal reactor or equilibrium models [*Steefel et al.*, 2005]. Fluid-mineral interactions occur inherently at the pore (micron) scale, and the representation of pore-scale heterogeneities in effective (averaged) models is not straightforward. This makes the study of reactive phenomena at the pore-scale particularly relevant. It provides information, not readily available from field data, that needs to be accounted for when modeling the behavior of reactive fluids percolating through sedimentary rocks. Understanding the relation between the degree of heterogeneity of a porous rock and the average dissolution rate is fundamental to advance the development of upscaling techniques for reactive flows and to model reactive phenomena at the field scale.

Carbonate reservoirs hold the majority of the world's oil reserves [*Schlumberger*, 2007], and calcite is the prevalent carbonate mineral in deep-sea sediments [*Morse and Arvidson*, 2002]. Carbonates are very reactive minerals, and alterations in the formation fluids (either natural or human-induced) can lead to dramatic variations in the petrophysical properties of the reservoir, e.g., *Schechter and Gidley* [1969]; *Noiriel et al.* [2009]; *Luquot and Gouze* [2009]; *Lamy-Chappuis et al.* [2014]. In this work, we explore the impact of the pore-space complexity of real porous media on the average dissolution rates, and on the permeability evolution via a first principles particle tracking approach that simulates carbonate dissolution at reservoir conditions (pressure is fixed at 10 MPa and temperature at 50°C, representative of an aquifer at 1 km depth).

A qualitative, macroscale description of dissolution patterns based on the nondimensional Péclet (*Pe*, the ratio of advection rate over diffusion rate) and Damköhler (*Da*, ratio of reaction rate over mass transport rate) numbers was proposed by *Daccord et al.* [1993] and later expanded and modified, e.g., *Budek and*

Szymczak [2012], *Golfier et al.* [2002], and *Maheshwari et al.* [2013]. Combining the experimental results of the dissolution of a porous medium made of salt grains with numerical simulations performed with a two-dimensional Darcy-scale model, *Golfier et al.* [2002] categorized three main regimes, as follows: (1) Compact (or face) dissolution, arising when the flow rate is low and the reaction rate high—$Pe \leq 2{\times}10^{-3}$ and $Da \geq 8{\times}10^{-4}$. Transport is diffusion-dominated and the acid is consumed close to the inlet. The rock is completely dissolved where injection occurs, and dissolution does not propagate throughout the sample. (2) Wormholing occurs when $Pe \geq 2{\times}10^{-3}$ and $Da \geq 8{\times}10^{-4}$. In comparison with the compact regime, the flow rate is higher, and highly conductive channels are etched through the rock, where all the reaction occurs. This regime is subdivided in dominant, conical, and ramified, depending on the geometric characteristics of the resulting pattern. (3) Uniform dissolution, characteristic of slow reactions ($Da \leq 8{\times}10^{-4}$), occurs when fresh reactant is carried away from the inlet, and reaction spreads throughout the sample. This categorization offers a fairly complete description of the behavior of porous media upon dissolution. However, it is based on centimeter-scale flow behavior, and does not account for pore-scale heterogeneity, nor does it distinguish different small-scale morphologies of the dissolution pattern. In particular, the terminology "uniform dissolution" is misleading; it does not imply that the entire pore space is equally accessible to the reactants or that the average reaction rate equals the intrinsic rate. Moreover, the transition lines between regimes are not universal, but are influenced by the system dimensionality, the pore-space morphology, and are sample-dependent. See, for instance, *Cohen et al.* [2008] who showed that the geometry of the domain has a strong influence on the wormholing pattern. While we use the boundary values from *Golfier et al.* [2002] to help contextualize our findings in terms of previous results, the exact location of the regime boundaries is sample-dependent. Any extrapolation from results obtained in a set of samples should be performed with caution.

Laboratory measured reaction rates are known to be, typically, several orders of magnitude higher than the ones estimated from field studies in natural systems. The observed reaction rates at the reservoir scale are affected by different physical and chemical heterogeneities that manifest themselves at different spatial scales, this explain the discrepancy between intrinsic rates (e.g., those measured in ideal reactors) and field rates. Among other factors, this discrepancy has been attributed to incomplete mixing of solutes [*Li et al.*, 2008], variations in fluid residence times [*Maher*, 2010], and the presence of physical and chemical heterogeneities [*Salehikhoo et al.*, 2013; *Steefel et al.*, 2005; *Ellis et al.*, 2011]. The impact of the velocity field heterogeneity on dissolution rates was studied by *Molins et al.* [2012] in two-dimensional systems. They showed that the average rate decreases when increasing the complexity of the pore space. Studying homogeneous reactions in different pore structures *Alhashmi et al.* [2015, 2016] showed that the effective reaction rate depends on the degree of mixing, flow field heterogeneity, and transport conditions. In this work, we quantify the reduction of average rates at the millimeter scale for monomineralic rocks caused by pore-scale physical heterogeneities.

Time-resolved pore-scale imaging of dissolution [*Menke et al.*, 2015] showed that, in the uniform dissolution regime, the average dissolution rate of a carbonate rock is one order of magnitude lower than the intrinsic rate. Further study [*Menke et al.*, 2016] demonstrated that for rocks with a more heterogeneous initial pore structure, dissolution in the same regime proceeded through the growth of high-flow channels in the rock, significantly restricting the volume over which reaction occurred, with average reaction rates around 100 times smaller than the batch values. This was termed a channelled dissolution regime. In this paper, we will confirm this conceptual picture and we will use pore-scale simulations, which in previous work were used to predict the results of pore-scale imaging experiments [*Pereira Nunes et al.*, 2016; *Menke et al.*, 2015], to obtain a quantitative estimate on the average dissolution rates of heterogeneous rocks (a bead pack, an oolite and a bioclastic limestone). We also provide estimates for the increase in the representative elementary volume (REV) after dissolution and show that changes in permeability are sample-dependent.

This paper is organized as follows. We start by describing the flow, transport, and reaction model proposed by *Pereira Nunes et al.* [2016]—section 2. Next, we discuss the characterization of transport and reaction in terms of the nondimensional Péclet and Damköhler numbers (section 3). A description of the samples and of the simulation strategy is found in sections 4 and 5. Section 6 presents the simulation results for the long-time behavior upon dissolution at high-flow rates. It is shown that the average dissolution rate depends on the rock heterogeneity and on the flow rate. Section 7 investigates the early time behavior and the permeability evolution at low-flow rates. Finally, section 8 summarizes our main results.

2. Fluid Flow, Transport, and Reaction

Here we summarize the assumptions and implementation of the particle-based dissolution method introduced by *Pereira Nunes et al.* [2016].

Solute transport is modeled with a particle (Lagrangian) approach. This method obtains transport characteristics by simulating individual stochastic particle trajectories, instead of solving directly the transport equations [*Kinzelbach*, 1988; *Tompson and Gelhar*, 1990; *Salamon et al.*, 2006]. The solute concentration is recovered by calculating the average number of particles in a reference volume at a given time. We adopt a hybrid scheme: particles are transported in an Eulerian flow field resulting from the numerical solution of the incompressible Navier-Stokes equations. Transport is divided into two steps: advection and diffusion. During advection the particles move along streamlines, which do not traverse solid voxels. Diffusion is modeled as a random particle motion, allowing particles to jump across streamlines and to cross the pore-solid interfaces, thus creating a flux of particles from the pores to the solids. This defines the reaction rate, as discussed in section 2.3.

2.1. Velocity Field and Permeability

The velocity field is obtained by numerically solving the incompressible Navier-Stokes equation in the voxels of segmented micro-CT images with a finite-volume method implemented with an open source library [*OpenFoam*, 2013; *Raeini et al.*, 2012; *Bijeljic et al.*, 2013a]:

$$\rho\left(\frac{\partial \vec{V}}{\partial t}+\vec{V}.\nabla\vec{V}\right)=-\nabla P+\mu\nabla^2\vec{V} \tag{1}$$

$$\nabla.\vec{V}=0 \tag{2}$$

where μ is the fluid viscosity, P is the pressure, ρ the fluid density, and $\vec{V}$ the velocity. The boundary conditions are constant pressure at the inlet and outlet faces and no-slip $\left(\vec{V}=0\right)$ at the interfaces.

The image-calculated permeability (k) is determined from Darcy's law:

$$k=\frac{L_s\mu Q}{A\Delta P} \tag{3}$$

where L_s is the sample length, A is the cross-sectional area, Q is the total flow rate at the sample outlet, and ΔP is the pressure drop.

2.2. Particle Transport

The displacement of a particle p after a time-step (Δt) has an advective and a diffusive contribution:

$$\Delta\vec{X}_p=\Delta\vec{X}_p^{adv}(\vec{V},\Delta t)+\Delta\vec{X}_p^{diff} \tag{4}$$

where $\Delta\vec{X}_p=\vec{X}_p(t+\Delta t)-\vec{X}_p(t)$ and $\vec{X}_p(t)$ is the position of a particle p at a time t.

2.2.1. Streamline Tracing and Tortuosity

During advection, the particles follow streamlines traced with the semianalytical method developed by *Pereira Nunes et al.* [2015]. This method is based on quadratic interpolations of the velocity field within each grid block, consistent with the numerical solution of equation (1) at grid faces and with the pore-scale boundary conditions: $\vec{V}=0$ at the solid interfaces. This semianalytical method eliminates numerical stability issues inherent in conventional time-stepping approaches and allows the time-step to be constrained by diffusion only.

Flow-weighted tracing of streamlines is used to estimate the hydraulic tortuosity (T) [*Duda et al.*, 2011]:

$$T=\frac{\langle L_{sl}\rangle}{L_x} \tag{5}$$

where $\langle L_{sl}\rangle$ is the average length of the streamlines and L_x is the sample length. The tortuosity provides a sample-scale estimative of the impact of pore-space geometry and flow field heterogeneity on the particle transport. High values correspond to more complex geometries.

2.2.2. Diffusion

Diffusive displacements are modeled with a random walk method. At each time-step, the diffusive jump of the particle is given by [*Benson and Meerschaert*, 2008]:

$$\Delta \vec{X}_p^{diff} = \lambda \left(\vec{\xi} - \frac{\vec{1}}{2} \right) \tag{6}$$

where

$$\lambda = \sqrt{24 D_m \Delta t} \tag{7}$$

and $\vec{\xi}$ is a vector of uniformly distributed random components. This generates a three-dimensional stochastic motion with mean-free path $\sqrt{6 D_m \Delta t}$, where D_m is the molecular diffusion coefficient. The simulation time-step is calculated by limiting the maximum diffusive jump. Imposed to be $l/2$, where l is the voxel length. This leads to:

$$\Delta t = \frac{l^2}{24 D_m} \tag{8}$$

2.3. Mineral Dissolution in the Particle Approach

Mineral dissolution is determined by the flux of particles through the pore-solid walls. The model assumes first-order kinetics, meaning that the reactive flux at the mineral surface is proportional to the particle concentration, and reaction-limited dissolution, implying that no significant concentration gradients develop in the vicinity of the surface.

Once a stationary state is reached, the diffusive flux equals the reactive flux at the surface. The reactive flux is determined by the intrinsic reaction rate r [mol.m^{-2}.s^{-1}], i.e., the rate free of mass transport limitations. Intrinsic rates are usually measured in batch reactors (stirred reactors closed to mass transfer) [*Pokrovsky et al.*, 2005; *Peng et al.*, 2015] and in this work we use both terms interchangeably. The diffusive flux in a fluid with reactant concentration C [n. of particles.m^{-3}] is determined by the average number of particles crossing the interface in a time step. By equating the number of mineral moles dissolved to the local flux of particles, it is possible to derive the number of particle hits (N_{hits}) required to dissolve one voxel comprised of N_{mol}^{voxel} moles of the dissolving mineral:

$$N_{hits} = \frac{\sqrt{6}}{4} \sqrt{\frac{D_m}{\Delta t}} \frac{C N_{mol}^{voxel}}{r} \tag{9}$$

This establishes a direct relationship between the intrinsic (batch) dissolution rate and the particle concentration without any adjustable parameters since the number of hits to dissolve is calculated in terms of a priori information, namely the intrinsic reaction rate (obtained from independent measurements) [*Peng et al.*, 2015], the diffusion coefficient, the time step, and the mineral density.

In practical implementations of the method, the number of particles is fixed, and when they react (collide with the solids), they are reinjected at the inlet. This creates an imbalance in the concentration profile. The reaction rate is equalized by adjusting dynamically the number of hits to dissolve as a function of the slice-averaged concentration. This is necessary to keep the ratio N_{hits}/C (and hence the reaction rate) constant. This will be discussed further in section 5.

In a first-order surface reaction, dissolution is proportional to the local flux of particles at the pore-solid walls, which in turn is determined by diffusion. The flux is calculated by counting the number of particles that cross from the surrounding pore voxels to a specific solid voxel. This model represents conditions under which the fluid is constantly out-of-equilibrium with respect to the rock. Once a particle crosses the solid-fluid interface it reacts (it is removed from the simulation) and the number of hits which that particular solid voxel has received is updated. After a certain number of hits (equation (9)), the solid voxel is fully dissolved into a pore voxel.

2.4. Calcite Dissolution

The main product of calcite (CaCO$_3$) dissolution in the presence of CO$_2$-saturated brines is Ca^{2+}, which is released in the aqueous phase. This dissolution kinetics has been extensively discussed elsewhere, e.g.,

Peng et al. [2015]; *Pokrovsky et al.* [2005]; *Chou et al.* [1989]. Throughout this work, we consider $r = 8.1 \times 10^{-4}$ mol.m^{-2}.s^{-1}, the rate corresponding to calcite dissolution in a CO_2-saturated brine at 10 MPa and 50°C [*Peng et al.*, 2015].

Pereira Nunes et al. [2016] introduced a model that describes the dissolution kinetics in terms of the concentration of a single kind of particle, which is, in turn, interpreted as the Ca^{2+} undersaturation, or the deviation from the equilibrium concentration, in the liquid phase. The fluid is in equilibrium with respect to the solid when $C = 0$; in this case, the flux of particles to the solids is zero and no dissolution occurs.

3. Description of Transport and Reaction: The Péclet and Damköhler Numbers

Péclet and Damköhler numbers are used to characterize reactive transport. The Péclet number (*Pe*) compares the rate of mass transfer due to advection to the rate of mass transfer by diffusion over a characteristic length (*L*):

$$Pe = \frac{qL}{\phi D_m} \qquad (10)$$

here $q = Q/A$ the Darcy velocity. For a porous rock, we adopt $L = \pi V / S_A$, where V is the volume of the sample and S_A is the area of the pore-solid interface [*Mostaghimi et al.*, 2012]. This is a good approximation for the effective diameter of the rock grains extended to cases where identification of a typical grain size is difficult, or impossible, such as in many carbonates. When $Pe > 1$, transport is advection-dominated.

The (advective) Damköhler number (*Da*) is the ratio of the advective time-scale and the reaction time-scale [*Lasaga*, 1998]. It is the ratio of the time to dissolve a volume V of a porous rock with molar density n [mol.m^{-3}] and surface area S_A over the advective time ($t_{adv} = L\phi/q$):

$$Da = \frac{\pi r \phi}{qn(1-\phi)} \qquad (11)$$

At the interfaces, $\vec{V} = 0$ and transport is diffusion-dominated. The product $PeDa$ is equivalent to the diffusive Damköhler number—the ratio between the reaction rate and the diffusion rate—and describes the dissolution kinetics. When $PeDa < 1$, the kinetics is reaction-limited, and when $PeDa > 1$ it is diffusion-limited.

As discussed in the introduction, behavior diagrams have been proposed to classify dissolution patterns observed in Darcy-scale simulations and experiments in terms of the *Pe* and *Da* numbers. While qualitatively correct and useful to interpret core-scale results, their direct application to pore-scale scenarios is not straightforward. This will be further explained in sections 6 and 7.

4. Sample Characterization

We selected three images of porous media with distinct geometries, petrophysical properties, and provenience to study the dynamics of carbonate dissolution: an artificial random packing of identical spheres, an Estaillades carbonate (a bioclastic limestone), and a Ketton oolite. The bead pack image is based on measurements of the bead centers in a monodisperse bead pack by *Finney* [1970], for which subsequent segmentation was performed by *Prodanovic and Bryant* [2006]. The Ketton and Estaillades images were acquired using a Versa XRM-500 X-Ray Microscope (Zeiss X-Ray Microscopy, Pleasanton, CA, USA) and segmented with a watershed algorithm [*Andrew et al.*, 2014; *Menke et al.*, 2015]. Both Estaillades and Ketton are mostly monomineralic rocks, composed of more than 95% calcite [*Andrew et al.*, 2014].

Figure 1 shows the pore space geometry and the corresponding computed velocity fields for the three samples. The grains in the Ketton carbonate are roughly spherical and the pores are well connected. There is a significant flow throughout almost the entire pore space in both Ketton and the bead pack. In comparison, Estaillades has a less connected pore space and the flow field is highly channelized. This is reflected in its tortuosity, the highest of the three samples studied. Table 1 summarizes image-calculated sample properties: porosity, permeability, tortuosity, and characteristic pore length.

Figure 2 shows the probability density function (PDF) of the horizontal velocity component. The bead pack has the narrowest distribution followed by Ketton and Estaillades, which has a much wider distribution.
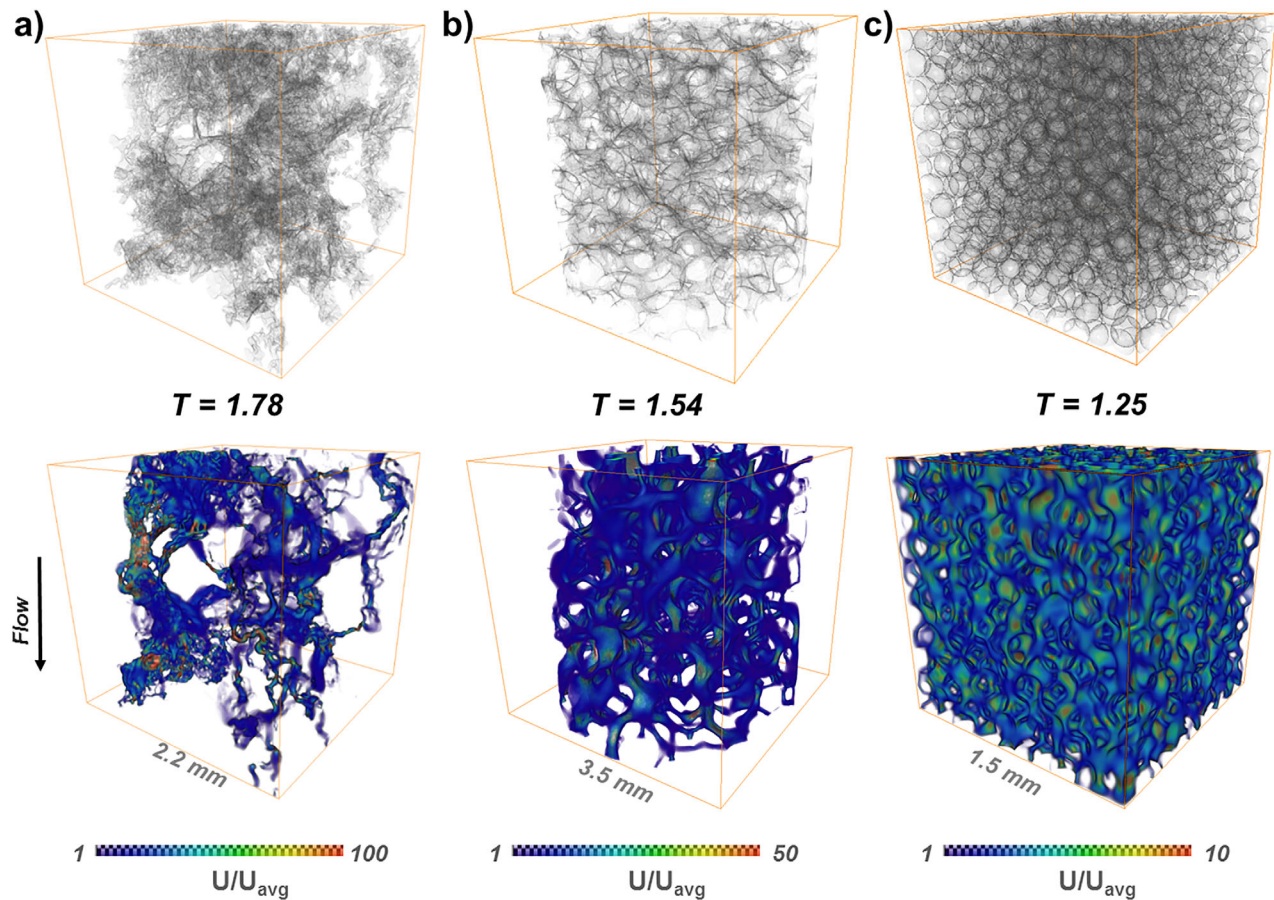
Figure 1. (top row) Surface of the solid grains, (bottom row) velocity fields, and corresponding tortuosities before reaction for (a) Estaillades limestone, (b) the Ketton oolite, and (c) the pack of spheres. The tortuosity (T, equation (5)) is higher in the Estaillades sample, which has the most heterogeneous flow field.

Wide velocity distributions are manifestations of the presence of significant stagnant zones, regions of slow flow, with restricted solute access in advection-controlled flows [*Bijeljic et al.*, 2013b]. Ultimately, this flow characteristic is responsible for the divergence between average rates and batch rates. Furthermore, the qualitative similarity between their corresponding PDFs explains why Ketton and bead pack exhibit a similar behavior upon dissolution, as discussed in section 6. From the geological perspective, the Ketton rock is an oolite, a limestone comprised of roughly spherical grains (ooids) of calcite albeit with significant cementation. This suggests that it retained some of its original features as a packing of spheres.

Subresolution porosity is accounted for by means of a factor that corrects the number of mineral moles in the solid voxels according to standard helium porosimetry measurements. The grain porosity (ϕ_{grain}), the porosity of the solid phase, is estimated by comparing the helium porosity (ϕ_{HP}) and the micro-CT porosity (ϕ):

$$\phi_{grain} = \frac{\phi_{HP} - \phi}{1 - \phi} \tag{12}$$

Based on *Andrew et al.* [2014], we calculate $\phi_{grain} = 0.12$ for Ketton and $\phi_{grain} = 0.22$ for Estaillades. The grain porosity is then used to calculate the effective number of calcite moles in the solid voxels:

Table 1. Summary of the Properties of the Studied Samples[a]

Sample	Lithology	ϕ (.)	k(D)	T	L (μm)	Dimensions	Voxel Size (μm)
Bead pack	Artificial	0.362	13.9	1.25	84	500×500×500	3.0
Estaillades	Limestone	0.119	0.5	1.75	269	650×650×650	3.3
Ketton	Limestone	0.163	13.3	1.54	420	455×451×461	7.6

[a]Porosity (ϕ), permeability (k), and the characteristic length (L) are image-calculated and the hydraulic tortuosity (T, equation (5)) is calculated from the semianalytical streamlines.
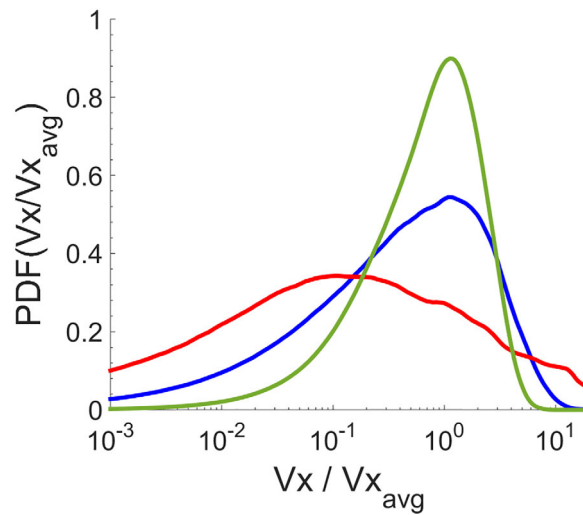
Figure 2. Velocity probability distributions—Estaillades limestone (red line), Ketton oolite (blue line), and the bead pack (green line). Of the three, Estaillades has the widest distribution, reflecting the very heterogeneous nature of its flow field. Ketton and the bead pack have more homogeneous velocity fields and narrower distributions.

$$N_{mol}^{voxel} = nl^3 (1 - \phi_{grain}) \qquad (13)$$

where l^3 is the voxel volume and $n = 2.71 \times 10^4$ mol.m^{-3} is the calcite molar volume [*Wenk and Bulakh*, 2004]. We have then: $N_{mol}^{voxel} = 10.6 \times 10^{-12}$ mol for Ketton, and $N_{mol}^{voxel} = 7.7 \times 10^{-13}$ mol for Estaillades. In the bead pack, $\phi_{grain} = 0$ and $N_{mol}^{voxel} = 7.3 \times 10^{-13}$ mol.

5. Simulation Strategy

The flow simulations are performed imposing an initially prescribed *Pe*, which is attained by establishing a pressure gradient that satisfies the desired Darcy velocity. 2.0×10^4 particles are injected with a flow weighted rule at the inlet and tracked until they either collide with a solid through diffusion or exit the domain. In both cases, a new particle is injected at the inlet, thus keeping the number of particles constant. The reaction rate is fixed (section 2.4), and the molecular diffusion coefficient is that of Ca^{2+}: $D_m = 7.5 \times 10^{-10}$ m^2.s^{-1} [*Luquot and Gouze*, 2009]. This results in: $PeDa = 1.8 \times 10^{-2}$ for the bead pack, $PeDa = 7.0 \times 10^{-2}$ for Ketton and $PeDa = 4.0 \times 10^{-2}$ for Estaillades. Dissolution is in the reaction-controlled regime: fast transport and slow reaction.

Following dissolution, the geometry of the pore space changes. Therefore, the velocity field must be updated. This is done at regular intervals when the bulk porosity increases by a fixed amount—$\Delta\phi \geq 0.001$. This is consistent with the scenario in which localized increases in porosity do not lead to a large variation in the global pressure field. The choice of $\Delta\phi$ is a compromise between computational performance and accuracy [*Pereira Nunes*, 2016]. Using smaller values of $\Delta\phi$ does not affect the results. The reaction rate is equalized throughout the sample by introducing a correction in the number of hits to dissolve. We replace the volumetric particle concentration (*C*) in equation (9) with the slice-averaged concentration $\bar{C}(s_x)$:

$$N_{hits}^{eff}(s_x) = \frac{\sqrt{6}}{4} \sqrt{\frac{D_m}{\Delta t}} \frac{\bar{C}(s_x) N_{mol}^{voxel}}{r} \qquad (14)$$

where s_x stands for the tomographic slice number in the flow direction. This ensures that the reaction rate (*r*) is constant and eliminates spurious boundary effects caused by the higher concentration of particles at the inlet.

The main steps of the algorithm are:

1. Solve the incompressible Navier-Stokes equation.
2. Flow weighted particle injection at the inlet.
3. Particle advection along semianalytical streamlines.
4. Particle diffusion by a random walk. When particle collides with a solid, kill it and reinject at the inlet. If the number of hits on any solid voxel is equal or larger than N_{hits}^{eff} (equation (14)), dissolve the voxel solid (change from solid to void) and update the porosity.
5. Repeat steps 3 and 4 for every particle and time step.
6. Update the flow field (solve the Navier-Stokes equation) when $\Delta\phi \geq 0.001$ and update the number of hits to dissolve—equation (14).
7. Repeat items 3–6 until the end of the simulation.

6. Results: Average Dissolution Rates at High Péclet Numbers

This section studies the asymptotic sample-averaged dissolution rates at high-flow rates (high Péclet number). We simulate the long-time behavior of Ketton, Estaillades, and the bead pack under two initial flow

Table 2. Simulation Parameters and Associated Macroscale Dissolution Regimes [*Golfier et al.*, 2002] for the Injection of 1000 PVI

	Pe	Da	PeDa	Macroscale Regime
Bead pack	10	1.8×10^{-3}	1.8×10^{-2}	Wormholing
	100	1.8×10^{-4}	1.8×10^{-2}	Uniform
Estaillades	10	4.0×10^{-3}	4.0×10^{-2}	Wormholing
	100	4.0×10^{-4}	4.0×10^{-2}	Uniform
Ketton	10	7.0×10^{-3}	7.0×10^{-2}	Wormholing
	100	7.0×10^{-4}	7.0×10^{-2}	Uniform

rates, corresponding to $Pe = 10$ and $Pe = 100$. Table 2 summarizes the simulation parameters and the expected dissolution regime according to the macroscale classification from *Golfier et al.* [2002]; dissolution is in the uniform regime for $Pe = 100$ and in the wormholing regime for $Pe = 10$.
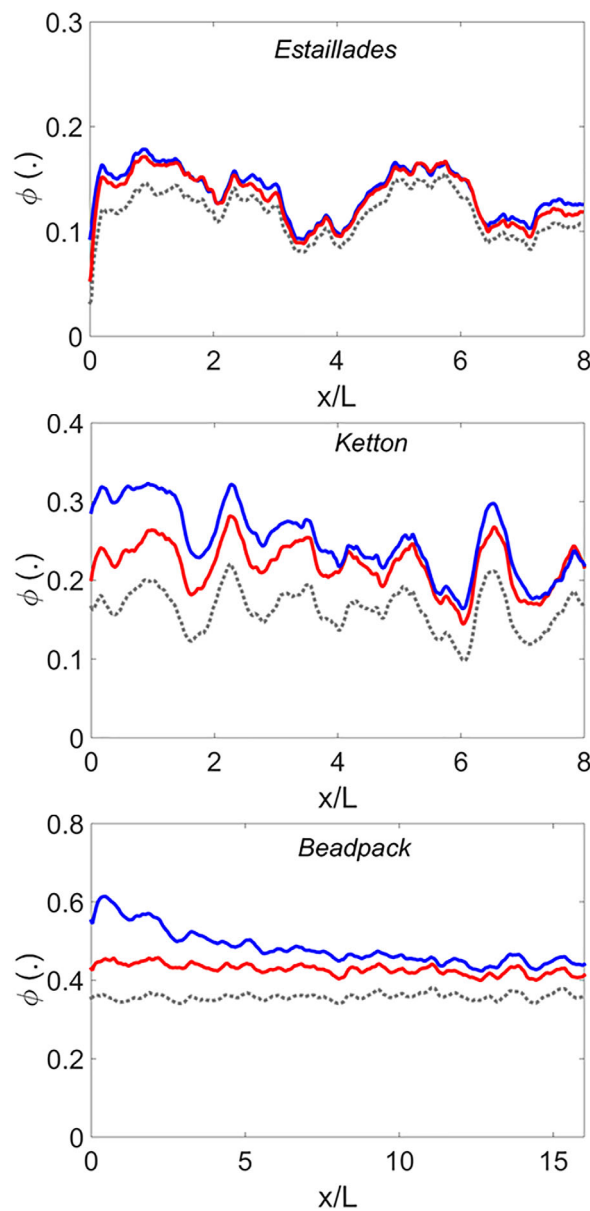

Figure 3. Slice-averaged porosity profiles along the direction of flow before injection (dashed grey) and after injecting 1000 pore volumes in Estaillades, Ketton, and the bead pack, from top to bottom. The red lines correspond to $Pe = 100$ and the blue ones to $Pe = 10$. The three samples experience an increase in porosity along the flow axis.

At the Darcy scale, the uniform dissolution regime is associated with slow reactions and high-flow conditions that favor the spreading of fresh reactants throughout the sample. Under these conditions, *Menke et al.* [2015] and *Pereira Nunes et al.* [2016] discussed how sample-scale transport limitations imposed by a heterogeneous flow field are responsible for a decrease of one order of magnitude in the average reaction rate when compared to the batch rate. It was shown that this flow and reaction regime, termed "uniform" in Darcy-scale studies, is actually a regime where the average dissolution rate is severely constrained by pore-scale heterogeneities.

When the flow rate is high, the average particle displacement is large enough to propagate the reaction throughout the sample, from inlet to outlet. We can then compute the average dissolution rate between times t and t' from the micro-CT surface area ($S_A(t)$) and the change in porosity ($\Delta\phi'$):

$$r^{eff} = \frac{\Delta\phi' V n}{(t'-t) S_A(t)} \quad (15)$$

The average rate as a function of the number of pore volumes injected (PVI) is investigated for the three samples while varying the flow rate.

The porosity profiles (the slice-averaged porosities along the direction of flow) before and after reaction are shown in Figure 3. The three samples experience an increase in porosity across the flow axis, evidencing that the flow rate is high enough to carry the solute throughout the samples. Since the residence time is higher for $Pe = 10$ than for $Pe = 100$, the increase in the bulk porosity is also higher, for the same amount of fluid injected. As a consequence of the increase in
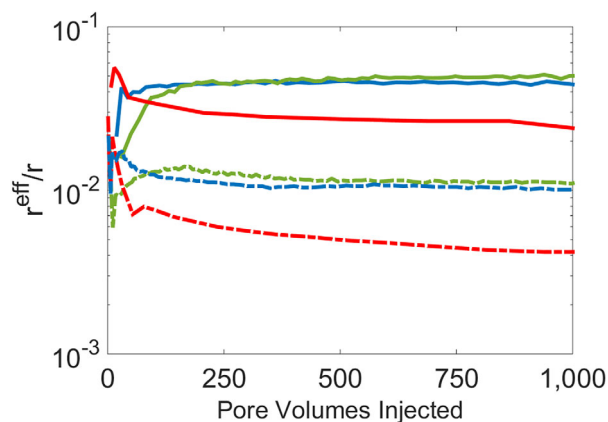
Figure 4. Ratio of the average reaction rate (equation (15)) over the batch reaction rate (*r*) during injection of a CO_2-saturated brine. The average rates for the more heterogeneous rock (Estaillades, in red) are lower than the rate of the relatively homogeneous ones (Ketton in blue and bead pack in green). Higher flow rates yield higher average reaction rates – $Pe = 100$, solid lines. The dashed lines are for $Pe = 10$.

porosity, the permeability also increases. In Estaillades, it starts from 0.5 D and reaches 8.4 D and 5.1 D after 1000 PVI, for $Pe = 10$ and $Pe = 100$, respectively. In Ketton, it goes from 13.3 D to 128.0 D and 70.9 D, for $Pe = 10$ and $Pe = 100$, respectively. In the bead pack, permeability increases from 13.9 D to 61.9 D and 31.8 D, for $Pe = 10$ and $Pe = 100$, respectively.

Figure 4 shows the ratio r^{eff}/r for the three samples under two initial flow rates, corresponding to $Pe = 10$ and $Pe = 100$. The Ketton and the bead pack samples (blue and green lines, respectively) have comparable average rates, a consequence of their broadly similar velocity fields (Figure 2), while the Estaillades sample has a lower rate. We contend that this is a manifestation of its heterogeneous velocity field, which causes a very inefficient sampling of the pore space. Large portions of the Estaillades pore space remain virtually unaffected by reactive transport, even after injecting 1000 PVI, Figure 5. In contrast, practically all of the pore space of the Ketton and bead pack is modified after injection of the reactive particles. The channelized nature of the Estaillades velocity field confines the flux of solute to very localized regions, thus limiting the spread of dissolution to preferential channels, as observed experimentally by *Menke et al.* [2016]. The other two, more homogeneous rocks, exhibit a much more uniform dissolution pattern, Figure 5.

Dissolution increases the connectivity and enlarges the pore throats, it is thus expected that the tortuosity (equation (5)) should decrease as a consequence. In fact, this is observed in the three samples. Following the injection 1000 PVI with initial $Pe = 100$, we observe that in the bead pack it decreases from $T = 1.25$ to 1.16, from $T = 1.54$ to 1.31 in Ketton, and from $T = 1.75$ to 1.32 in Estaillades.

Transport is advection-dominated and the presence of stagnant zones inhibits the access of the reactants to a significant part of the reactive surface. Moreover, a high-flow rate (Figure 4, solid lines, $Pe = 100$) results in higher average reaction rates in comparison with the lower flow rate (Figure 4, dashed lines, $Pe = 10$). The increase from $Pe = 10$ to $Pe = 100$ results in an increase of almost one order of magnitude in the reaction rate for the three samples. Zones that have low velocity when $Pe = 10$ become accessible to the particles as the velocity rises, resulting in a more even spread of the dissolution front, Figure 6.
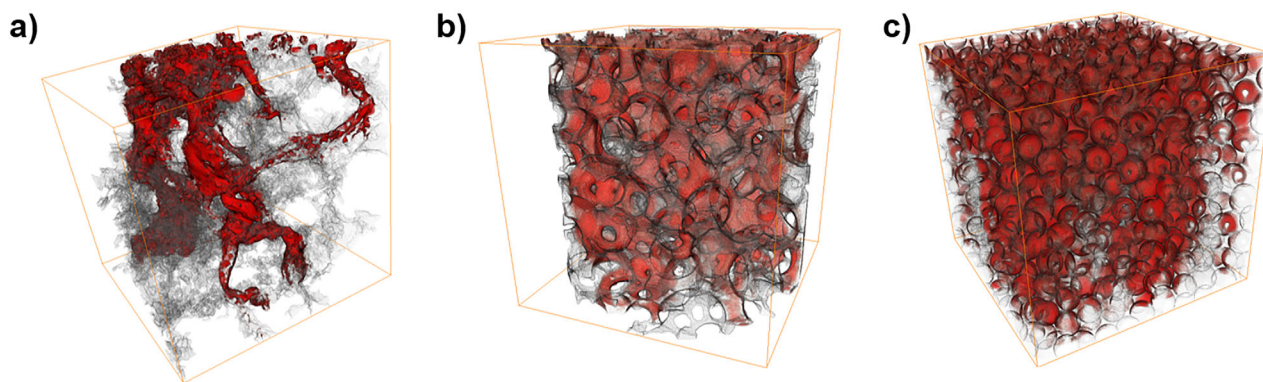

Figure 5. Dissolved portions (shown in red) superimposed with the original pore space (light grey) after injecting 1000 pore volumes, starting with an initial Péclet number of 100. Dissolution in the Estaillades sample (a) is more channelized and restricted than in the Ketton (b) and bead pack (c) samples. This is a result of the flow field heterogeneity (Figure 1) and results in a lower average dissolution rate, as seen in Figure 4.
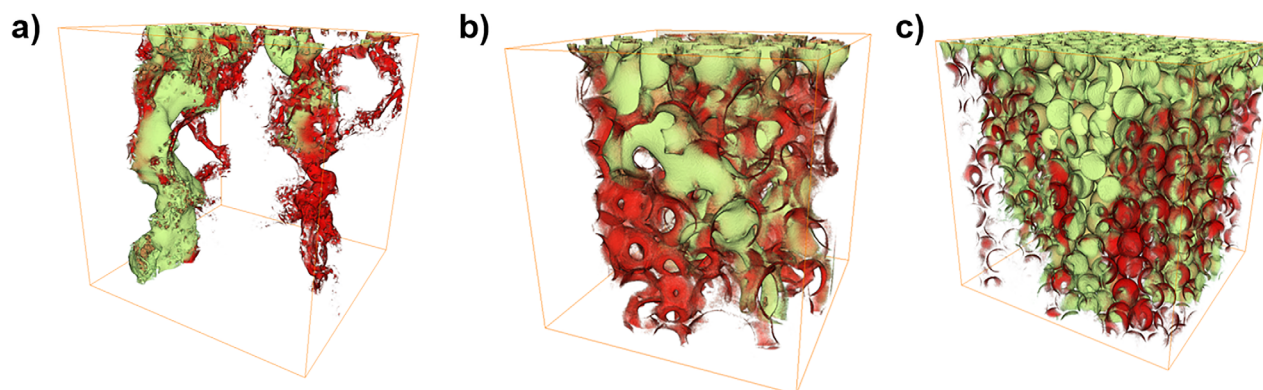
Figure 6. Time-lapse images after injecting 1000 pore volumes. Dissolution varies with the flow rate, green corresponds to $Pe = 10$, and red to $Pe = 100$. In the (a) Estaillades, a secondary channel develops when increasing the flow rate, while in the (b) Ketton and (c) bead pack, high-flow rates yield a more uniform dissolution.

Despite being classified as in the wormholing regime according to the Pe and Da numbers, characteristic wormhole-like channels, where macroscale paths are etched through the rock, are not present in the dissolution pattern for $Pe = 10$, for any of the samples studied, Figure 6. Instead, reaction proceeds through the widening of preexisting flow channels, with some reaction throughout the sample. These channels are not wormholes, as they are a pore-scale phenomenon occurring in a slow reaction regime ($Da \ll 1$) and do not retain all the reactant: dissolution proceeds along the length of the sample through the growth of fast-flow pathways, not from the etching of new sample-scale holes. Qualitatively similar behavior is seen for both $Pe = 100$ and $Pe = 10$.

The understanding of the reaction dynamics can be further strengthened by analysing the evolution of the velocity field distribution. As shown in Figure 5, while the long-term dissolution of Ketton and bead pack alters most of the original pore space, significant parts of Estaillades remain largely unchanged. Figure 7 shows the corresponding PDFs of velocities before and after the injection of 1000 PVI for the three samples for $Pe = 100$. Estaillades evolves into a bimodal distribution, where the stagnant zones are mostly preserved by the reactions, while the high-flow regions become more pronounced. This is a markedly different behavior from the one exhibited by the Ketton and bead pack samples, in which the broad characteristics of the distributions remain. The bead pack PDF is virtually unchanged, and the Ketton PDF becomes narrower with a more pronounced peak. This narrowing of the distribution, in the case of Ketton, indicate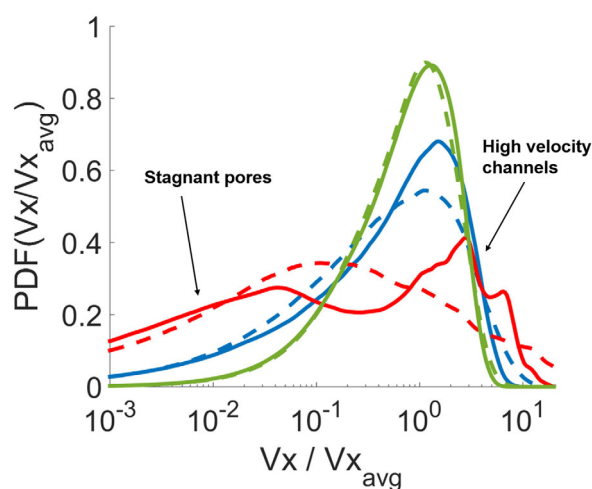s that the pore space is becoming less complex and more well connected as a result of dissolution: more pores have velocities close to the average. The opposite is happening in Estaillades; dissolution preferentially enlarges preexisting fast flow channels, while keeping the stagnant zones unchanged. The resulting flow field is more heterogeneous and its distribution is bimodal.

Overall, these results are in qualitative agreement with the experimental results of *Menke et al.* [2016], who showed that dissolution-induced changes in the velocity field depend on the initial pore structure—in more heterogeneous rocks, dissolution occurs preferentially in channels (regions of fast flow) leaving stagnant zones largely unaffected.

Figure 7. PDFs of velocities, before (dashed lines) and after injection of 1000 pore volumes at $Pe = 100$ (solid lines). The bead pack (green) is mostly unaffected, Ketton (blue) becomes narrower with a more pronounced peak. The PDFs of the Estaillades (red lines) rock show the development of high-velocity channels.

The representative elementary volume (REV) is defined as the minimum sample volume above which statistical variations of a given property become negligible [*Bear*, 1988]. Its
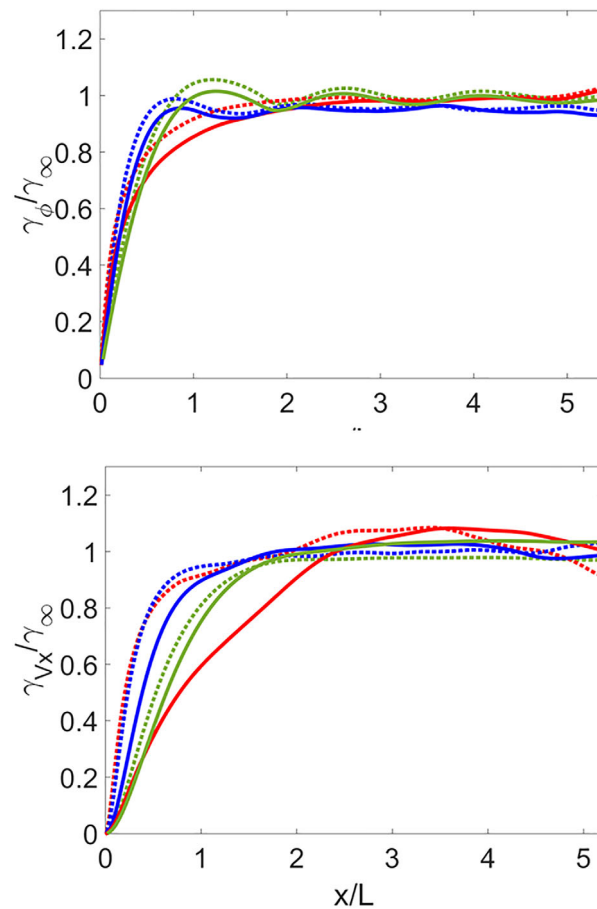
Figure 8. (top) Normalized porosity and (bottom) velocity variograms before (dashed lines) and after injection (solid lines) of 1000 pore volumes with $Pe = 100$. All the three samples—Estaillades (red), Ketton (blue), and the bead pack (green)—experienced an increase in the correlation length, an indicative of larger REVs. The variograms are plotted against horizontal distance over the initial characteristic length (L), Table 1.

value is property dependent, i.e., the permeability REV is not necessarily the same as the porosity REV, the former being normally larger due to long-range correlations in the flow field. Macroscale, image-calculated properties are meaningful only when obtained from volumes larger than the REV. As a consequence of dissolution, both the average pore-size and the connectivity increase. It is thus expected that the REV also increases with the emergence of new structures, particularly if dissolution channels are formed. A useful way of estimating the REV is provided by the empirical (semi)variogram, which describes the behavior of data correlation with distance. For a given property p, it is defined as:

$$\gamma_p(h) = \frac{1}{2N(h)} \sum_{i=1}^{N(h)} [p(x_{i+h}) - p(x_i)]^2 \quad (16)$$

where h is the distance between two observations and $N(h)$ is the number of observations such that $|p(x_{i+h}) - p(x_i)| = h$ [*Doyen*, 2007]. It measures the dissimilarity between data separated by a distance h. Once the variogram reaches a plateau, the data are uncorrelated. Figure 8 shows the porosity and velocity variograms before and after reaction. The variograms are plotted as a function of the horizontal distance (distance measured from inlet) divided by the initial characteristic length. All the three samples experience an increase in the correlation length for both porosity and horizontal velocity: larger REVs

are necessary to characterize these rocks after dissolution. This effect is stronger in Estaillades, where we see a large increase in the velocity correlation length. This is explained by the intense channelization of the pore space, which preserves the correlation of velocity. The effect of the flow and reaction in Estaillades is to enlarge high-flow channels and decrease tortuosity, therefore, increasing the similarity between velocities at different points inside the channel. A simple analogy is to consider the flow field inside a tube: if the velocity does not change longitudinally, as each point on a streamline is perfectly correlated with the previous one.

Even though the flow and reaction regime is the same for all three samples considered—$Pe \gg 1$ and $PeDa \ll 1$—we observe that the average rate is both rate and sample-dependent. For Estaillades, the most heterogeneous sample, the average rates are consistently lower than the ones for the more homogeneous Ketton and bead pack, Figure 4.

The heterogeneous nature of the flow field causes an uneven distribution of the reactants throughout the pores, thus restricting dissolution to regions with significant intake of solute. Accordingly, dissolution is more uniform in the two samples with more uniform velocity fields. However, even in these cases, the average reaction rate is still one order of magnitude lower than the batch rate.

7. Results: Initial Pore-Structure and Dissolution at Low Péclet Numbers

While the previous section focused on the asymptotic behavior of the average dissolution rates at high Péclet number and low Damköhler number conditions, this section studies the early time behavior and the

Table 3. Simulation Parameters and Associated Macroscale Dissolution Regimes [*Golfier et al.*, 2002] for the Injection of 10 PVI

	Pe	Da	$PeDa$	Macroscale Regime
Estaillades	1	4.0×10^{-2}	4.0×10^{-2}	Dominant wormhole
	2	2.0×10^{-2}	4.0×10^{-2}	Dominant wormhole
	5	8.0×10^{-3}	4.0×10^{-2}	Ramified/Dominant wormhole
	10	4.0×10^{-3}	4.0×10^{-2}	Ramified/Dominant wormhole
Ketton	1	7.0×10^{-2}	7.0×10^{-2}	Dominant wormhole
	2	3.5×10^{-2}	7.0×10^{-2}	Dominant wormhole
	5	1.4×10^{-2}	7.0×10^{-2}	Dominant wormhole
	10	7.0×10^{-3}	7.0×10^{-2}	Ramified/Dominant wormhole

influence of the initial pore geometry on the permeability evolution of Ketton and Estaillades at low-flow rates (low Péclet number), see Table 3 for the simulation parameters.

The penetration length of a reactive particle inside a sample is dependent on the Péclet number. Our results show that, for $Pe = 1$ and $Pe = 2$, and injecting 10PVI, dissolution is limited to regions close to the inlet. This means that, for a fixed number of injected pore volumes, if the injection rate is low enough, dissolution will not propagate throughout the sample.

Figure 9 shows the slice-averaged relative porosity difference in Ketton and in Estaillades along the direction of flow for four initial injection rates, corresponding to $Pe = 1, 2, 5,$ and 10. In both samples, the difference is concentrated close to the inlet for the lowest rates ($Pe = 1, 2$), and moves toward the outlet as the rate increases, i.e., the transport of reactants in the pore space is more effective and dissolution spreads throughout the rock. Note, however, that the penetration length is higher in Estaillades than in Ketton. This is due to the channelized characteristic of the Estaillades flow field, which favors the development of a localized dissolution around a preexistent channel, an effect that is more pronounced for higher Pe, Figure 10. In both samples, even at low Pe, distinct channels are etched through the rock.

The sample-dependent difference in the range of the dissolution (Figures 9 and 10) should have an obvious impact on the permeability behavior. This is illustrated in Figure 11, which compares the evolution of the permeability as a function of porosity for both rocks. The alterations in Ketton are concentrated at the inlet, and do not connect across the sample, even for $Pe = 10$. Consequently, despite the increase in porosity, the permeability remains essentially unaffected for the flow rates considered. The opposite happens in Estaillades, where we observe the widening of a channel extending from inlet to outlet. This occurs at the lower flow rate corresponding to $Pe = 5$. This localized enlargement of a highly conductive channel connecting inlet and outlet is responsible for a marked
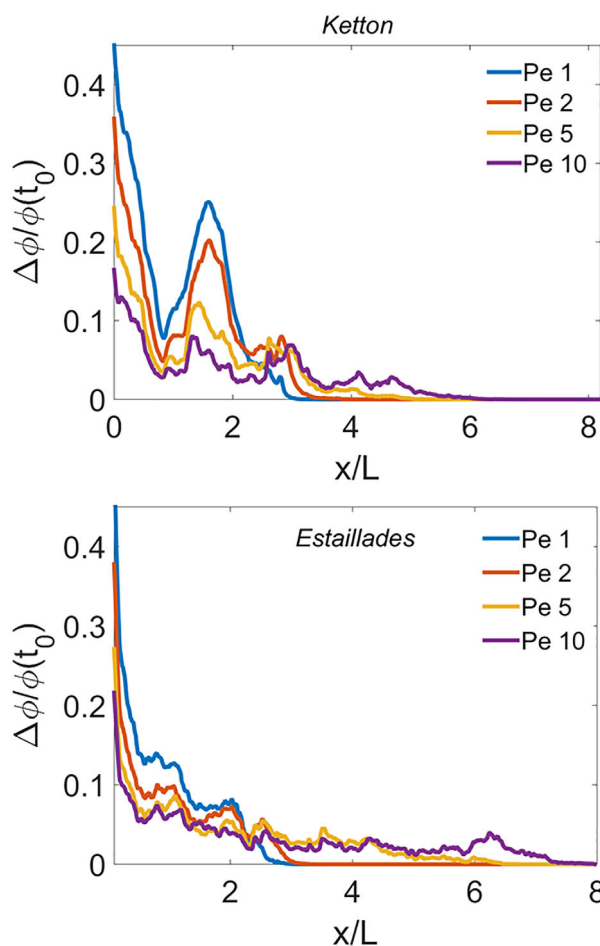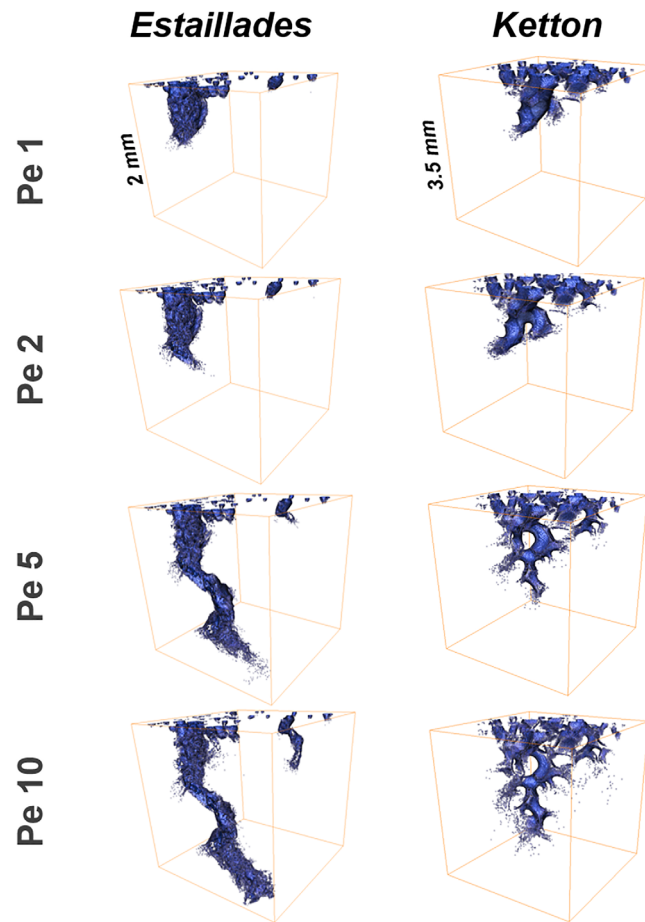

Figure 9. Slice-averaged relative porosity difference *versus* distance over the characteristic length (L), after injecting 10 pore volumes in (top) Ketton and in (bottom) Estaillades. Dissolution penetrates further for the higher flow rates, particularly in Estaillades, the more channelized rock. Flow is from left to right. Ketton is 8.2 L in length and Estaillades 7.9 L.

Figure 10. Dissolution fronts following the injection of 10 pore volumes for four flow rates, corresponding to $Pe=1$, 2, 5, and 10. For low-flow rates ($Pe=1$, 2), reaction is contained close to the inlet. Increasing the injection rate ($Pe=5$, 10), the channelized nature of flow in the Estaillades focuses the reaction into high-flow channels, with a greater impact on permeability.
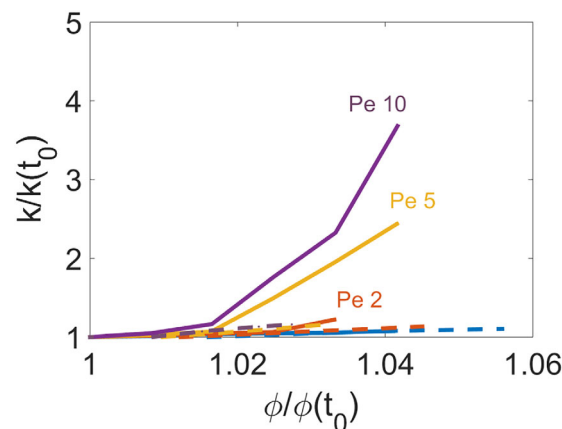

Figure 11. Permeability evolution for Ketton (dashed lines) and Estaillades (solid lines) following the injection of 10 pore volumes with four different flow rates, corresponding to $Pe = 1$, 2, 5, and 10. The permeability of Ketton is largely unaffected for the range of flow rates considered: a consequence of dissolution being concentrated at the inlet. In contrast, Estaillades shows a marked increase in permeability for the higher rates: a result of fast flow channels dissolving.

increase in permeability. Furthermore, the nonuniqueness of the permeability versus porosity curve evidenced by Figure 11 has potential impacts for the modeling of dissolution in reservoir-scale models. These are currently constructed based on the assumption that the entire permeability field is a well-defined function of the porosity [*Steefel et al.*, 2014]. However, Figure 11 shows that such assumption does not hold. Instead, the permeability behavior upon dissolution is a function not only of porosity, but also of the pore-space morphology and the flow rate. For instance, the distribution of tracer transit times, and consequently of the flow rate and Péclet number, is known to be very wide in heterogeneous reservoirs [*Di Donato et al.*, 2003; *Di Donato and Blunt*, 2004]. This suggests that an adequate description of the evolution of permeability upon dissolution cannot be obtained in terms of a single permeability versus porosity relation.

8. Conclusions

This paper presented a modeling study to illustrate the influence of the initial pore structure on the transport of reactants in porous rocks and the associated impact on the sample-averaged fluid-solid reaction rates. A more complex pore space gives rise to a more heterogeneous flow field, which imposes limitations on the transport of reactive solute at the millimeter scale. These pore-scale constraints manifest themselves collectively as a sample-scale discrepancy of, at least, one order of magnitude between average reaction rates and batch reaction rates, even in relatively homogeneous rocks. Another indication of the transport-controlled kinetics at the sample scale is the dependency of the average rates on the flow rates—higher flow rates yield higher average reaction rates.

As illustrated in section 6, the underlying complexity of the pore geometry (and of its corresponding flow field) defines the average reaction rate in asymptotic times, even in the so-called uniform dissolution regime—$Pe \gg 1$, $PeDa \ll 1$. Despite being useful in several circumstances,

this commonplace definition ("uniform") does not describe what is happening at the pore scale. Specifically, in heterogeneous rocks, we observe the preferential dissolution of fast-flow channels, and the flow and dissolution regime is more accurately described as channelled, rather than uniform. This was also reported in an imaging experiment tracking the pore-space evolution during reactive transport [*Menke et al.*, 2016].

The distinct evolution of the velocity PDFs of rocks with different pore characteristics is a strong indication that a description of dissolution patterns solely based on the nondimensional numbers *Pe* and *PeDa* misses important features of the reaction dynamics in real rocks. Previous work has focused on reproducing core experiments and adopted a Darcy-scale continuum representation of the porous medium. This approach fails to account for pore-scale heterogeneities and does not fully describe the dynamics of dissolution in terms of the pore structure [*Daccord et al.*, 1993; *Golfier et al.*, 2002; *Maheshwari et al.*, 2013]. This paper is a contribution in this direction: through computational modeling we investigated the interdependency of the dissolution process and the geometry of the pore space, which, in turn, impacts the average reaction rate and the dependence between permeability and porosity. Furthermore, while our focus was on the dissolution of calcitic carbonates, reservoirs of commercial interest are usually formed by a combination of calcite and dolomite (and other minerals in smaller concentrations). The simulation method employed here can be readily expanded to treat chemically heterogeneous rocks by using a multi-phase segmentation (e.g., pores + calcite + dolomite) and attributing different reaction rates to each kind of solid voxel.

Fluid-solid reactions are broadly characterized as either surface or transport-controlled. This a useful description in batch reactors, closed systems in which the reactants are readily available in the solution in contact with the mineral surface. We argue that such description is incomplete when considering reactive transport in porous media. There is one extra factor to be taken into account: the geometry of the pore space, which may limit the transport of solute to the solid surface at the sample scale. This means that a reaction can be surface-controlled at the pore scale (a rough analogy would be to consider every pore as a batch reactor) but transport-controlled at the sample scale. This was the case exemplified here.

References

Alhashmi, Z., M. Blunt, and B. Bijeljic (2015), Predictions of dynamic changes in reaction rates as a consequence of incomplete mixing using pore scale reactive transport modeling on images of porous media, *J. Contam. Hydrol.*, *179*, 171–181, doi:10.1016/j.jconhyd.2015.06.004.

Alhashmi, Z., M. Blunt, and B. Bijeljic (2016), The impact of pore structure heterogeneity, transport and reaction conditions on fluid/fluid reaction rate studied on images of pore space, *Transp. Porous Media*, doi:10.1007/s11242-016-0758-z, in press.

Andrew, M., B. Bijeljic, and M. J. Blunt (2014), Pore-scale imaging of trapped supercritical carbon dioxide in sandstones and carbonates, *Int. J. Greenhouse Gas Control*, *22*, 1–14, doi:10.1016/j.ijggc.2013.12.018.

Bear, J. (1988), *Dynamics of Fluids in Porous Media*, Dover Civ. and Mech. Eng. Ser., Dover, N. Y.

Benson, D. A., and M. M. Meerschaert (2008), Simulation of chemical reaction via particle tracking: Diffusion-limited versus thermodynamic rate-limited regimes, *Water Resour. Res.*, *44*, W12201, doi:10.1029/2008WR007111.

Bijeljic, B., A. Raeini, P. Mostaghimi, and M. J. Blunt (2013a), Predictions of non-Fickian solute transport in different classes of porous media using direct simulation on pore-scale images, *Phys. Rev. E*, *87*, 013011, doi:10.1103/PhysRevE.87.013011.

Bijeljic, B., P. Mostaghimi, and M. J. Blunt (2013b), Insights into non-Fickian solute transport in carbonates, *Water Resour. Res.*, *49*, 2714–2728, doi:10.1002/wrcr.20238.

Budek, A., and P. Szymczak (2012), Network models of dissolution of porous media, *Phys. Rev. E*, *86*, 056,318, doi:10.1103/PhysRevE.86.056318.

Chou, L., R. M. Garrels, and R. Wollast (1989), Comparative study of the kinetics and mechanisms of dissolution of carbonate minerals, *Chem. Geol.*, *78*(34), 269–282, doi:10.1016/0009-2541(89)90063-6,.

Cohen, C. E., D. Ding, M. Quintard, and B. Bazin (2008), From pore scale to wellbore scale: Impact of geometry on wormhole growth in carbonate acidization, *Chem. Eng. Sci.*, *63*(12), 3088–3099, doi:10.1016/j.ces.2008.03.021.

Daccord, G., O. Liétard, and R. Lenormand (1993), Chemical dissolution of a porous medium by a reactive fluid: II. Convection vs reaction, behavior diagram, *Chem. Eng. Sci.*, *48*(1), 179–186, doi:10.1016/0009-2509(93)80294-Z.

Di Donato, G., and M. J. Blunt (2004), Streamline-based dual-porosity simulation of reactive transport and flow in fractured reservoirs, *Water Resour. Res.*, *40*, W04203, doi:10.1029/2003WR002772.

Di Donato, G., E.-O. Obi, and M. J. Blunt (2003), Anomalous transport in heterogeneous media demonstrated by streamline-based simulation, *Geophys. Res. Lett.*, *30*(12), 1608, doi:10.1029/2003GL017196.

Doyen, P. (2007), *Seismic Reservoir Characterization: An Earth Modelling Perspective, Educ. Tour Ser.*, EAGE Publ., Amsterdam, Netherlands.

Duda, A., Z. Koza, and M. Matyka (2011), Hydraulic tortuosity in arbitrary porous media flow, *Phys. Rev. E*, *84*, 036,319, doi:10.1103/PhysRevE.84.036319.

Ellis, B., C. Peters, J. Fitts, G. Bromhal, D. McIntyre, R. Warzinski, and E. Rosenbaum (2011), Deterioration of a fractured carbonate caprock exposed to co2-acidified brine flow, *Greenhouse Gases*, *1*(3), 248–260, doi:10.1002/ghg.25.

Finney, J. L. (1970), Random packings and the structure of simple liquids. i. the geometry of random close packing, *Proc. R. Soc. London, Ser. A*, *319*(1539), 479–493, doi:10.1098/rspa.1970.0189.

Golfier, F., C. Zarcone, B. Bazin, R. Lenormand, D. Lasseux, and M. Quintard (2002), On the ability of a Darcy-scale model to capture wormhole formation during the dissolution of a porous medium, *J. Fluid Mech.*, *457*, 213–254, doi:10.1017/S0022112002007735.

Kinzelbach, W. (1988), The random walk method in pollutant transport simulation, in *Groundwater Flow and Quality Modelling, NATO ASI Ser.*, vol. 224, edited by E. Custodio, A. Gurgui, and J. Ferreira, pp. 227–245, Springer, Netherlands, doi:10.1007/978-94-009-2889-3_15.

Lamy-Chappuis, B., D. Angus, Q. Fisher, C. Grattoni, and B. W. D. Yardley (2014), Rapid porosity and permeability changes of calcareous sandstone due to CO_2-enriched brine injection, *Geophys. Res. Lett.*, *41*, 399–406, doi:10.1002/2013GL058534.

Lasaga, A. C. (1998), *Kinetic Theory in the Earth Sciences*, 1st ed., Princeton Univ. Press, Princeton, N. J.

Li, L., C. I. Steefel, and L. Yang (2008), Scale dependence of mineral dissolution rates within single pores and fractures, *Geochim. Cosmochim. Acta*, *72*(2), 360–377, doi:10.1016/j.gca.2007.10.027.

Luquot, L., and P. Gouze (2009), Experimental determination of porosity and permeability changes induced by injection of CO2 into carbonate rocks, *Chem. Geol.*, *265*(12), 148–159, doi:10.1016/j.chemgeo.2009.03.028.

Maher, K. (2010), The dependence of chemical weathering rates on fluid residence time, *Earth Planet. Sci. Lett.*, *294*(1-2), 101–110, doi: 10.1016/j.epsl.2010.03.010.

Maheshwari, P., R. Ratnakar, N. Kalia, and V. Balakotaiah (2013), 3-d simulation and analysis of reactive dissolution and wormhole formation in carbonate rocks, *Chem. Eng. Sci.*, *90*(0), 258–274, doi:10.1016/j.ces.2012.12.032.

Menke, H. P., B. Bijeljic, M. G. Andrew, and M. J. Blunt (2015), Dynamic three-dimensional pore-scale imaging of reaction in a carbonate at reservoir conditions, *Environ. Sci. Technol.*, *49*(7), 4407–4414, doi:10.1021/es505789f.

Menke, H. P., M. Andrew, M. Blunt, and B. Bijeljic (2016), Reservoir condition imaging of reactive transport in heterogeneous carbonates using fast synchrotron tomography: Effect of initial pore structure and flow conditions, *Chem. Geol.*, *428*, 15–26, doi:10.1016/j.chemgeo.2016.02.030.

Molins, S., D. Trebotich, C. I. Steefel, and C. Shen (2012), An investigation of the effect of pore scale flow on average geochemical reaction rates using direct numerical simulation, *Water Resour. Res.*, *48*, W03527, doi:10.1029/2011WR011404.

Morse, J. W., and R. S. Arvidson (2002), The dissolution kinetics of major sedimentary carbonate minerals, *Earth Sci. Rev.*, *58*, 51–84, doi: 10.1016/S0012-8252(01)00083-6.

Mostaghimi, P., B. Bijeljic, and M. J. Blunt (2012), Simulation of flow and dispersion on pore-space images, *SPE J.*, *17*, 1131–1141.

Noiriel, C., L. Luquot, B. Madé, L. Raimbault, P. Gouze, and J. van der Lee (2009), Changes in reactive surface area during limestone dissolution: An experimental and modelling study, *Chem. Geol.*, *265*(12), 160–170, doi:10.1016/j.chemgeo.2009.01.032

OpenFoam (2013), *OpenFoam*. [Available at http://www.openfoam.org.]

Peng, C., J. P. Crawshaw, G. C. Maitland, and J. M. Trusler (2015), Kinetics of calcite dissolution in CO_2-saturated water at temperatures between (323 and 373) K and pressures up to 13.8 MPa, *Chem. Geol.*, *403*, 74–85, doi:10.1016/j.chemgeo.2015.03.012.

Pereira Nunes, J. P. (2016), Pore-scale modelling of carbonate dissolution, PhD thesis, Imperial College London, London, U. K.

Pereira Nunes, J. P., B. Bijeljic, and M. Blunt (2015), Time-of-flight distributions and breakthrough curves in heterogeneous porous media using a pore-scale streamline tracing algorithm, *Transp. Porous Media*, *109*(2), 317–336, doi:10.1007/s11242-015-0520-y.

Pereira Nunes, J. P., M. J. Blunt, and B. Bijeljic (2016), Pore-scale simulation of carbonate dissolution in micro-CT images, *J. Geophys. Res. Solid Earth*, *121*, 558–576, doi:10.1002/2015JB012117.

Pokrovsky, O. S., S. V. Golubev, and J. Schott (2005), Dissolution kinetics of calcite, dolomite and magnesite at 25C and 0 to 50 atm pCO2, *Chem. Geol.*, *217*, 239–255, doi:10.1016/j.chemgeo.2004.12.012.

Prodanovic, M., and S. L. Bryant (2006), A level set method for determining critical curvatures for drainage and imbibition, *J. Colloid Interface Sci.*, *304*(2), 442–458, doi:10.1016/j.jcis.2006.08.048.

Raeini, A. Q., M. J. Blunt, and B. Bijeljic (2012), Modelling two-phase flow in porous media at the pore scale using the volume-of-fluid method, *J. Comput. Phys.*, *231*(17), 5653–5668, doi:10.1016/j.jcp.2012.04.011.

Salamon, P., D. Fernàndez-Garcia, and J. J. Gómez-Hernández (2006), A review and numerical assessment of the random walk particle tracking method, *J. Contam. Hydrol.*, *87*, 277–305, doi:10.1016/j.jconhyd.2006.05.005.

Salehikhoo, F., L. Li, and S. L. Brantley (2013), Magnesite dissolution rates at different spatial scales: The role of mineral spatial distribution and flow velocity, *Geochim. Cosmochim. Acta*, *108*, 91–106, doi:10.1016/j.gca.2013.01.010.

Schechter, R. S., and J. L. Gidley (1969), The change in pore size distribution from surface reactions in porous media, *AIChE J.*, *15*(3), 339–350, doi:10.1002/aic.690150309.

Schlumberger (2007), *Carbonate Reservoirs: Meeting Unique Challenges to Maximize Recovery*. [Available at http://www.slb.com.]

Steefel, C. I., D. J. DePaolo, and P. C. Lichtner (2005), Reactive transport modeling: An essential tool and a new research approach for the earth sciences, *Earth Planet. Sci. Lett.*, *240*(34), 539–558, doi:10.1016/j.epsl.2005.09.017.

Steefel, C. I., et al. (2014), Reactive transport codes for subsurface environmental simulation, *Comput. Geosci.*, *19*(3), 445–478, doi:10.1007/s10596-014-9443-x.

Tompson, A. F. B., and L. W. Gelhar (1990), Numerical simulation of solute transport in three-dimensional, randomly heterogeneous porous media, *Water Resour. Res.*, *26*(10), 2541–2562, doi:10.1029/WR026i010p02541.

Wenk, H.-R., and A. Bulakh (2004), *Minerals: Their Constitution and Origin*, 1st ed., Cambridge Univ. Press, Cambridge, U. K.